Comparative Study for Electrochemical and Single-Cell Performance of a Novel MXene-Supported Platinum–Ruthenium Catalyst for Direct Methanol Fuel Cell Application

Norulsamani Abdullah[1], Saidur Rahman[1,2,*], Azran Mohd Zainoodin[3], Navid Aslfattahi[4]

[1]*Research Center for Nano-Materials and Energy Technology (RCNMET), School of Science and Technology, Sunway University, Bandar Sunway, Petaling Jaya, 47500, Selangor Darul Ehsan, Malaysia*
[2] *Department of Engineering, Lancaster University, Lancaster, LA1 4YW, UK*
[3] *Fuel Cell Institute, National University of Malaysia, 43600 UKM Bangi, Selangor, Malaysia*
[4]*Department of Fluid Mechanics and Thermodynamics, Faculty of Mechanical Engineering, Czech Technical University in Prague, Technická 4, 160 00, Prague, Czech Republic*

Corresponding authors: saidur@sunway.edu.my

ABSTRACT

Direct methanol fuel cell (DMFC) is one of the reliable sources of energy owing to numerous benefits it offers and its suitability for portable electronic applications. Therefore, this study aims to overcome the main issues confronting anodic electrocatalyst part by introducing the novel formulation of platinum–ruthenium (PtRu) bimetal into the 2D $Ti_3C_2T_x$ structure to boost the electrocatalytic activity and single-cell performance. A comparative study for electrochemical measurement and DMFC performance is conducted between as-synthesized electrocatalyst PtRu/$Ti_3C_2T_x$ and two other electrocatalysts, PtRu/C and Pt/C. This comparative study between electrocatalyst revealed that PtRu/$Ti_3C_2T_x$ exhibits the highest electrochemical surface area (55 $m^2\ g^{-1}$), electrocatalytic and intrinsic activity (449 mA mg_{PtRu}^{-1}/ 1.36 mA cm_{ECSA}^{-2}), carbon monoxide tolerance (1.56), and smallest charge-transfer resistance (2.66 Ω) compared with other electrocatalysts. Furthermore, the validation by DMFC single-cell test showed that PtRu/$Ti_3C_2T_x$ electrocatalyst improves the performance almost 70 % compared to the Pt/C electrocatalyst. This excellent electrochemical and single-cell performance of PtRu/$Ti_3C_2T_x$ electrocatalyst

validates its potential to be one of the promising candidates for the anodic electrocatalyst in DMFC application.

Keywords: MXene, Anodic electrocatalyst, Electrochemical measurement, Single cell performance, Direct methanol fuel cell.

Nomenclatures:

Q	Charge density (C)
Γ	Charge constant of proton monolayer on the Pt (C m_{Pt}^{-2})
W_{Pt}	Pt loading (g_{Pt})
I_f	Forward oxidation peaks (mA cm^{-2})
I_b	Reverse oxidation peaks (mA cm^{-2})
η	Overpotential in the Tafel region (V)
i	Current density in the Tafel region (mA cm^{-2})
a	Ion exchange current density, a (mA cm^{-2})
b	Tafel slope (mV dec^{-1})
R	Gas constant (J mol^{-1} K^{-1})
T	Temperature (K)
F	Faraday constant (C mol^{-1})
α	Charge transfer coefficient
W_e	Electrocatalyst loading (mg cm^{-2})
m_{de}	Mass of deposited electrocatalyst (mg)
A_{iGCE}	Inner-active area of GCE (cm^2)

1. INTRODUCTION

Reliable and sustainable sources of energy are a vital aspect of our everyday life. The most current energy sources provide energy via combustion of fossil fuel which adversely impacts the planet [1]. A new technology of energy production must therefore be developed to overcome these problems. Direct methanol fuel cell (DMFC) is one of the most attractive technologies to produce reliable source of energy. Improvement of this technology will make a better and environment-friendly energy source. DMFC technology has garnered massive attention owing to the numerous benefits it offers, including high power density, energy efficiency and reliability, ease of fuel handling and charging, rapid start-up and simple system, and zero noise pollution [2, 3]. This energy technology is also a promising candidate for the portable power sources application such as cellular phones, notebook computers, and other portable electronic equipment [4-7]. Other than that, it is also categorized as an electrochemical energy storage which has gained tremendous popularity among the research community [8].

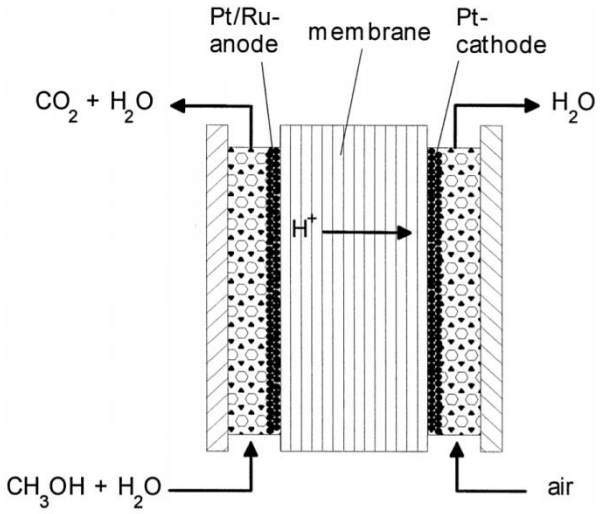

Figure 1: The general principal and illustration of DMFC technology [9].

DMFC is an electrochemical cell in which the energy of a reaction between fuel (methanol) is converted directly and continuously into electrical energy. Figure 1 illustrates the basic structure and principal of a single-cell DMFC system. A DMFC system typically consists of three main compartments, namely, anode electrode, membrane, and cathode electrode. The combination of these compartments is called as membrane electrode assembly (MEA), which is the heart of a DMFC system. All the main reaction occurs in this MEA, where the chemical reactions for anode and cathode electrodes are as follows [10]:

Anode Reaction: $CH_3OH + H_2O \rightarrow CO_2 + 6H^+ + 6e^-$

Cathode Reaction: $3/2\ O_2 + 6H^+ + 6e^- \rightarrow 3H_2O$

Overall Reaction: $CH_3OH + 3/2\ O_2 \rightarrow H_2O + CO_2$

A mixture of methanol and water as a fuel is fed into the system. Then, the mixture reaches the anode catalyst layer, which consists of anode electrocatalyst layer, where the methanol oxidation reaction (MOR) occurs. The reaction then produces carbon dioxide and a number of protons and electrons. The diffusion of proton from anode to cathode electrode occurs through the membrane layer. In addition, water as one of by-products is produced by reacting with oxygen. At the same time, electrons travel across the external circuit to function as a power source [11]. The use of methanol as a fuel in the transport sector can solve some of the issues faced by other alternative fuels, among them storage and distribution constraints, where it can use the existing petrol infrastructure with minor modifications [12-13]. Although some articles state the high price of methanol fuel, it can be categorized as less expensive (energy per unit) by providing a higher volumetric and gravimetric energy density than compressed hydrogen (at 1000 bar) and even liquid hydrogen [12]. Besides that, methanol also has toxicity compared to other alternative fuels [13]. In terms of fuel processing, the main raw materials for methanol are coal and natural gas,

which go through environmentally unfriendly processes. However, methanol production from renewable energy sources has been started in recent years, albeit with less efficiency [12]. More improvements in green methanol production can be made in the coming years to ensure that this fuel can be an attractive long-term solution.

Despite its merits, DMFC technology has certain short comings, which result in poor cell performance. The most noteworthy short comings are slow kinetic reaction, catalyst poisoning, stability and durability, and methanol cross-over [14]. First three issues are attributable to electrocatalyst side, especially anodic electrocatalyst, where the main kinetic reaction takes place. The anode electrocatalyst must possess high catalytic activity, and platinum (Pt) is the most suitable material for this technology. However, this metal has low tolerance toward the intermediate carbonaceous species, like carbon monoxide (CO), which is formed during the reaction. This intermediate species leads to catalyst poisoning and limits the anodic reaction rate, as well as reduces the cell performance [14]. Therefore, researchers have attempted to modify or replace the anodic electrocatalyst in order to achieve high cell performance [15-19].

Among different improvements proposed by various researchers, the combination of ruthenium (Ru) and Pt exhibits the highest compatibility for MOR performance. This material helps in lowering catalyst poisoning by increasing the formation of OH_{ads} on absorption sites, and it reacts with CO to form the CO_2 and H^+ [20]. Although the PtRu bimetal can act as main catalyst for DMFC, the catalyst support still requires attention as the commercial catalyst support, carbon (C), cannot provide high surface area and low utilization of a catalyst. This situation leads to a slow MOR, along with reduction in the kinetic reaction rate and cell performance. In the past decade, tremendous development has been made by researchers to bring the suitable material as a catalyst support for DMFC technology. The catalyst support for MOR

should have large surface area, strong catalyst–catalyst support interaction, and good corrosion tolerance and electrical conductivity [21].

One of the latest and widely studied materials is two dimensional material (2D), where graphene is one of the most common material used as catalyst support in electrochemical energy conversion system [22]. However, potentiality of graphene is spoiled by the serious stacking issue due to the Π–Π interaction between sheets, which leads towards major loss of electrochemical active surface area, limiting the ionic transport as well as impairing the system performance [23-25]. Other than that, the simple chemistry of pure graphene makes it electrochemically inert to most catalytic reactions that limits the synergistic coupling effect between metal and carbon matrix [26]. Since this is a critical issue related to electrochemical performance, a newcomer in the group of 2D materials, $Ti_3C_2T_x$, also known as MXene, has gained attention among researchers. This material can be categorized into ceramic and metal-like 2D materials and has unique properties, including high electrical conductivity and chemical stability [27], rapid ion intercalation and transport [28], and large surface area [29]. Additionally, the entire base plane of MXene is able to participate in the catalytic process which promotes high current density [28]. Particularly, the present of transition metal core layer, Ti, in MXenes provides fast electron transport through the electrode, and is an important property in enhancing the catalytic activity [28, 30]. MXenes also exhibit high hydrophilicity and metallicity properties due to the present of –OH group and transition metal, makes them suitable as supports for dispersing and stabilizing metal catalysts [31]. In addition, the surface of MXene that filled with transition metal atoms and functional groups, will produce interfacial charge transfer and lattice mismatch, which helps to form a unique heterojunction catalyst with combination of other metal catalyst [31]. These properties make MXenes have great potential to be used as catalyst supports

for fuel cells and other energy conversion systems [32]. The compatibility in this technology is proven by several studies conducted recently on electrocatalysts of Pd/$Ti_3C_2T_x$ [31], Pt/$Ti_3C_2T_x$ [33], and MoS_2QDs@$Ti_3C_2T_x$QDs@MWCNTs [34]. However, the combinations of PtRu bimetal and $Ti_3C_2T_x$ 2D material structure have not been explored yet. This novel electrocatalyst with superior properties of all material is expected to overcome the catalyst problem, such as catalyst poisoning and slow kinetic reactions.

Thus, this study investigated the novel combination of PtRu bimetal with $Ti_3C_2T_x$ 2D MXene for methanol oxidation reaction in DMFC application. This is the first work to report the fabrication of MEA involved $Ti_3C_2T_x$-based electrocatalyst for DMFC application. This is also the first time a comparison study between as-synthesized electrocatalyst, PtRu/$Ti_3C_2T_x$, with the commonly used electrocatalyst of PtRu/C and Pt/C to investigate potentiality of MXene based composite electrocatalyst. The elemental and morphological properties of electrocatalyst are characterized. The electrochemical measurement for electrochemical active surface area (ECSA), electrocatalytic activity, CO tolerance, and Tafel analysis are performed for all electrocatalysts. The resistance of charge transfer and equivalent model circuit for MOR is also reported for the first time for the as-synthesized electrocatalyst. The DMFC single-cell performance for the electrocatalyst is measured to validate the real potential of material to be a promising electrocatalyst for this technology. This performance is the first finding not only for PtRu/$Ti_3C_2T_x$ electrocatalyst but also for the MXene-based electrocatalyst. The single-cell performance of PtRu/$Ti_3C_2T_x$ exhibits almost 70 % increment compared with Pt/C electrocatalyst. This excellent finding indicates that PtRu/$Ti_3C_2T_x$ has high potential to replace the commercial electrocatalyst for DMFC application to overcome some of the challenges this technology is facing.

2. MATERIALS, SAMPLE PREPARATION, CHARACTERIZATION TECHNIQUE, ELECTRODE-MEMBRANE FABRICATION, AND SINGLE-CELL PERFORMANCE SET UP

2.1 Materials and Chemicals

Chloroplatinic acid (H_2PtCl_6, 37.5 % content) and ruthenium (III) chloride ($RuCl_3$, 45 – 55 % content) as precursors for Pt and Ru, respectively, were received from Sigma Aldrich, Germany. Furthermore, sodium borohydride ($NaBH_4$, 99 %), isopropyl alcohol (IPA, 99.8 %), and Nafion solution D520 (5 wt. %) were purchased from Sigma Aldrich, Germany, Chemiz, Malaysia and Chemours.com, respectively. The carbon black (C, Vulcan XC 72), as a catalyst support for other electrocatalyst, and Nafion 117 membrane, as a membrane for single-cell performance, was obtained from Fuel Cell Store, USA.

2.2 Preparation of Electrocatalysts

$Ti_3C_2T_x$ catalyst supports were synthesized using etching method by Aslfattahi et al. [35], where ammonium hydrogen difluoride (NH_4HF_2) acted as an etching agent. Chemical reduction method was used to deposit the main catalysts, 21 wt% of Pt and Ru with 1:1 atomic ratio, on the 79 wt.% of $Ti_3C_2T_x$ catalyst support. The composition of PtRu and $Ti_3C_2T_x$ is based on our previous optimization study [36]. Isopropyl Alcohol (IPA) (200 mL) and deionized water, with 1:1 volume ratio, were mixed with $Ti_3C_2T_x$. This mixture was homogenously sonicated at room temperature. Next, the catalyst support solution was transferred onto a hot plate, and main catalysts precursors were added and continuously stirred for another 30 min. pH value of the mixture was adjusted up to 8 by using NaOH (0.5 mol L^{-1}). Then, the temperature of the mixture was increased up to 80 ^oC. $NaBH_4$ (50 mL, 0.2 mol L^{-1}) was added dropwise as reducing agent

into the mixture and continuously stirred for another 1 hr. After that, the mixture was cooled until room temperature was reached. The mixture was separated using centrifuge at 15,000 rpm for 15 min and repeatedly washed using deionized water. The deposited materials were collected and dried overnight at 80 ºC under vacuum condition. Mortar and pestle were used to refine the dry material into the fine powder. The fine powder is known as PtRu/$Ti_3C_2T_x$ electrocatalyst. The same method was used to prepare PtRu/C and Pt/C electrocatalysts.

2.3 Physical Characterization of Electrocatalysts

PtRu/$Ti_3C_2T_x$, PtRu/C, and Pt/C underwent several physical characterizations to identify certain properties of the electrocatalysts. X-ray diffraction (XRD), which is a microstructural analysis method, was utilized to identify the phase, crystallinity, orientation, and dimension of material. The analysis was conducted using X-ray diffractometer (D8 Advance/Bruker AXS Germany) that was operated at 40 kV and 20 mA using powdered sample at range of angle between 2 º to 60 º with 2θ. The crystallite size of all elements was obtained using Eva Software (software for analyzing XRD), where it was calculated based on Debye-Scherrer equation as follow:

$$\text{Crystallite size} = 0.98\alpha/\beta\cos\theta \qquad \text{Eq. (1)}$$

Where α is wavelength of the X-ray, β is width of the peak at halfheight, and θ is angle at the peak. Then, field emission scanning electron microscope (FESEM, Hitachi SU8010, Japan) was done to visualize the surface morphology of the samples. The detailed material morphology, with the dimension of interlayer spacing was identified using transmission electron microscopy (TEM, Tecnai G^2 20 S-Twin, FEI Company USA). Meanwhile, the elemental distribution of the electrocatalysts sample was carried out using scanning electron microscopy (SEM, TESCAN VEGA3, Czech Republic) with AZtec analysis software, Oxford Instrument, UK. In addition, X-

ray photoelectron spectroscopic analysis (XPS, Kratos AXIS ULTRA DLD, Japan) was carried out to identify the type of element, and chemical state of electrocatalyst.

2.4 Electrochemical Measurement of Electrocatalyst

The electrochemical analysis of different type of electrocatalysts was conducted using several electrochemical measurements. Three types of measurements, namely, cyclic voltammetry (CV), linear sweep voltammetry (LSV), and electrochemical impedance spectroscopy (EIS), were performed. The CV measurement is divided into two types: CV profile and CV curve. The profile was measured to estimate the active surface area produced by the catalyst, which is also known as ECSA. The ECSA data were obtained from the CV profile in the acidic media of 0.5 mol L^{-1} H_2SO_4 with potential range of − 0.2 to 1.0 V versus Ag/AgCl at scan rate of 20 mV s^{-1}. The ECSA value was calculated by using Eq. 2, where Q is a charge density with the consideration of double layer capacitance (the integration of area under the graph), Γ is a charge required for proton monolayer adsorption on Pt (2.1 C m_{Pt}^{-2}), and W_{Pt} is a Pt mass loading.

$$ECSA = Q/\Gamma.W_{Pt} \quad \text{Eq. (2)}$$

Furthermore, the electrocatalytic activity and CO tolerance of the electrocatalysts were obtained from CV curve of CH_3OH (2.8 mol L^{-1}) and H_2SO_4 (0.5 mol L^{-1}). The scan rate for CV curve was noted to be 20 mV s^{-1}, while potential ranges were between − 0.2 to 1.0 V versus Ag/AgCl. LSV was conducted to analyze the electron kinetic transfer of electrocatalysts via Tafel plot. The LSV curve was measured in the solution of CH_3OH (2.8 mol L^{-1}) and H_2SO_4 (0.5 mol L^{-1}), in the potential range - 0.1 – 1.0 V versus Ag/AgCl at scan rate of 20 mV s^{-1}. The Tafel analysis is extracted using the Eq. 3:

$$\eta = a + b\log(i) \quad \text{Eq. (3)}$$

Where η is overpotential, i is current density, a is ion exchange current density, and b is Tafel slope. The charge-transfer coefficient, α, is calculated using Eq. 4:

$$b = 2.3\, RT/\alpha F \qquad \text{Eq. (4)}$$

Where R, T, and F represent the gas constant, temperature, and Faraday constant, respectively. Both CV and LSV were conducted under nitrogen environment. The interface electrical resistance of the material was measured via EIS in galvanostatic mode. The range of sweeping frequencies was between 100 kHz and 1 Hz, in the solution of CH_3OH (2.8 mol L^{-1}) and H_2SO_4 (0.5 mol L^{-1}). The CH_3OH concentration for electrochemical measurement was determined using optimum CH_3OH concentration value for $PtRu/Ti_3C_2T_x$ by Abdullah et al. [36].

All the electrochemical measurements were performed using potentiostat/galvanostat (Interface 1010E; max. applied current (±1 A) and potential (±12 V), Gamry Instruments, USA), accompanied by three-electrode system. The electrode system consists of three types of electrodes, namely, working electrode (glassy carbon electrode, GCE with inner-active diameter of 3 mm), reference electrode (Ag/AgCl), and counter electrode (Pt wire). The inner-active area of working electrode was calculated using equation of area of circle ($A_{iGCE} = \pi r^2$, where r is the inner-active radius of electrode). The electrocatalyst ink was prepared by dispersing IPA, deionized water, and Nafion solution D520 with 1: 4.75: 4.75 ratios using a probe sonicator. The ink was sonicated for 15 min or until well homogenous in room condition. The electrocatalyst ink with a loading of 0.4 mg cm^{-2} was dropped onto the working electrode surface area, referred to as the inner-active area of working electrode. The electrocatalyst loading was calculated using Eq. 5:

$$W_e = m_{de}/A_{iGCE} \qquad \text{Eq. (5)}$$

Where W_e is electrocatalyst loading, m_{de} is the mass of deposited electrocatalyst, and A_{iGCE} is the inner-active area of GCE. The working electrode was dried at room temperature for 1 hr before being further dried for 30 min at 70 ^oC. It was then ready to be used for the electrochemical measurement.

2.5 Fabrication of Membrane Electrode Assembly

Casting of gas diffusion layer (GDL), followed by gas diffusion electrode (GDE) and membrane deposition were performed for the fabrication of membrane–catalyst layer. The carbon cloth and Nafion 117 is acted as a backing layer and membrane layer. Meanwhile, the carbon black is used in GDL; PtRu/$Ti_3C_2T_x$, PtRu/C and Pt/C electrocatalyst in GDE anode; and Pt/C commercial electrocatalyst in GDE cathode. First, carbon cloth was pre-treated with 5 wt. % polytetrafluoroethylene (PTFE) to achieve hydrophobicity. Then, the carbon cloth was coated with carbon black to form the GDL layer, where the IPA and 5 wt. % Nafion solution were added to the carbon black powder. The slurry was casted onto the carbon cloth using the brush method and dried for 1 hr at 100 ^oC. After that, anode catalyst layer was coated on the GDL, where the electrocatalysts were mixed with IPA, deionized water, and Nafion solution in the vial. The mixture was dispersed using an ultrasonic crusher until homogenized and applied on top of the GDL layer using filter and pump method and dried for 1 hr at 100 ^oC. The procedure is repeated for the cathode layer. The Nafion membranes were simultaneously pretreated using H_2O_2 and H_2SO_4. The GDE of anode and cathode electrodes were sandwiched with Nafion membrane and assembled using a hot press for 180 s with temperature of 135 ^oC and pressure of 12.5 kg f cm^{-2}. The MEA was then ready to be used for testing single-cell performance.

2.6 Single-Cell Performance

DMFC single-cell performance testing was conducted in a passive state at room temperature using potentiostat/galvanostat (WonATech, Korea). A 4 cm^2 active area of MEA with 4 mg cm^{-2} catalyst loading was placed in the single-cell housing, where the anode part faced methanol tank. The assembled cell is activated overnight with 2 mol L^{-1} methanol before available to be used in single-cell performance. The full schematic diagram for the fabrication of MEA and single-cell performance is illustrated in Figure 2. 2.8 mol L^{-1} CH_3OH fuel was used for this performance testing, as for the electrochemical measurement above [36], and the polarization curve of the electrocatalyst was obtained.

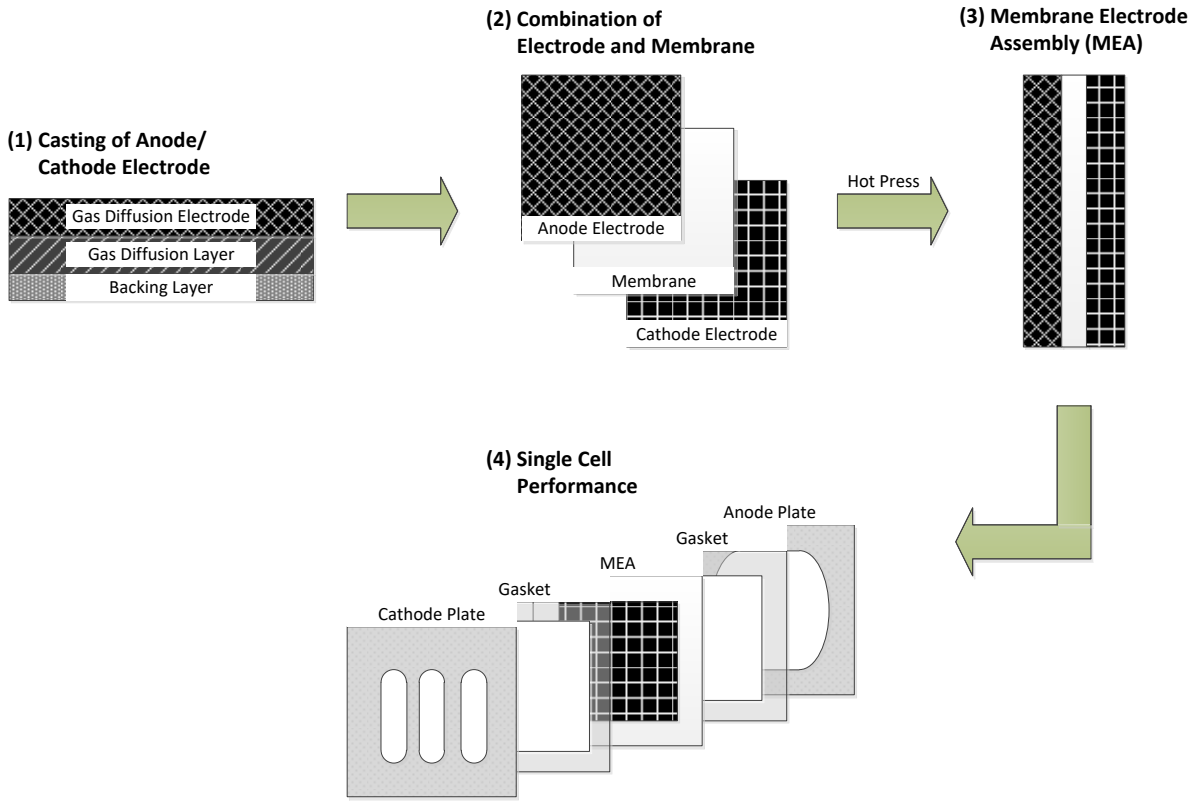

Figure 2: The full schematic diagram for the fabrication of MEA and single-cell performance.

3. RESULTS AND DISCUSSION

3.1 Physical Characterization of Electrocatalysts

Pattern and structure of crystal for all electrocatalysts, PtRu/$Ti_3C_2T_x$, PtRu/C, and Pt/C, were analyzed using XRD analysis, operated using X-ray diffractometer, within 2 ^{o} – 60 ^{o} with 2θ (see Figure 3). The XRD pattern for PtRu/$Ti_3C_2T_x$ electrocatalyst showed the diffraction peak for all elements needed, namely, Pt, Ru, and Ti_3C_2. The diffraction peak at 8.5 ^{o} (0 0 2) and 28 ^{o} (0 0 8) represent Ti_3C_2 element for synthesizing MXene using NH_4HF_2 as etching agent [37]. This element exists in hexagonal structure – the real crystallography structure for Ti_3C_2 element [32]. The elements Pt and Ru produced three peaks in the range of 39 ^{o} to 49 ^{o}. The Pt element had diffraction peak at 40 ^{o} (1 1 1) and 46.2 ^{o} (2 0 0), while Ru element had the same at 43.7 ^{o} (1 0 1). The Pt and Ru elements exist in cubic and hexagonal structure, respectively. The diffraction pattern for PtRu/C electrocatalyst reveals the existence of Pt and Ru elements at the same peak as PtRu/$Ti_3C_2T_x$ electrocatalyst. Meanwhile, C element appeared at diffraction peak of 40.4 ^{o} (1 1 1) and in cubic structure. The Pt/C electrocatalyst also shows the peak for both Pt and C. The diffraction peak for both elements is equivalent to the peak at other electrocatalysts. Therefore, the XRD data verified that $Ti_3C_2T_x$, Pt, and Ru were present in the sample.

Crystallite size for all elements present in the electrocatalyst sample is encapsulated as shown in Table 1. The crystallite size obtained from the XRD analysis for PtRu/$Ti_3C_2T_x$, PtRu/C, and Pt/C are between 9.17 – 15.62 nm, 9.84 – 16.17 nm, and 7.48 – 12.71 nm, respectively. From the XRD data as well, the expected interlayer spacing value for all electrocatalysts and their elements were recorded, and the value for all elements were observed to be below 10.38 Å (1.038 nm). Furthermore, the percentage of crystallinity shows that Pt/C electrocatalyst has highest percentage with 52.8 % of crystallinity, followed by PtRu/$Ti_3C_2T_x$ and PtRu/C. Based on

several research outcomes, the low percentage of crystallinity show great effect to the catalytic activity [38, 39]. This is due to its low charge transfer resistance caused by the high density of unsaturated sites present on its disordered surface [40].

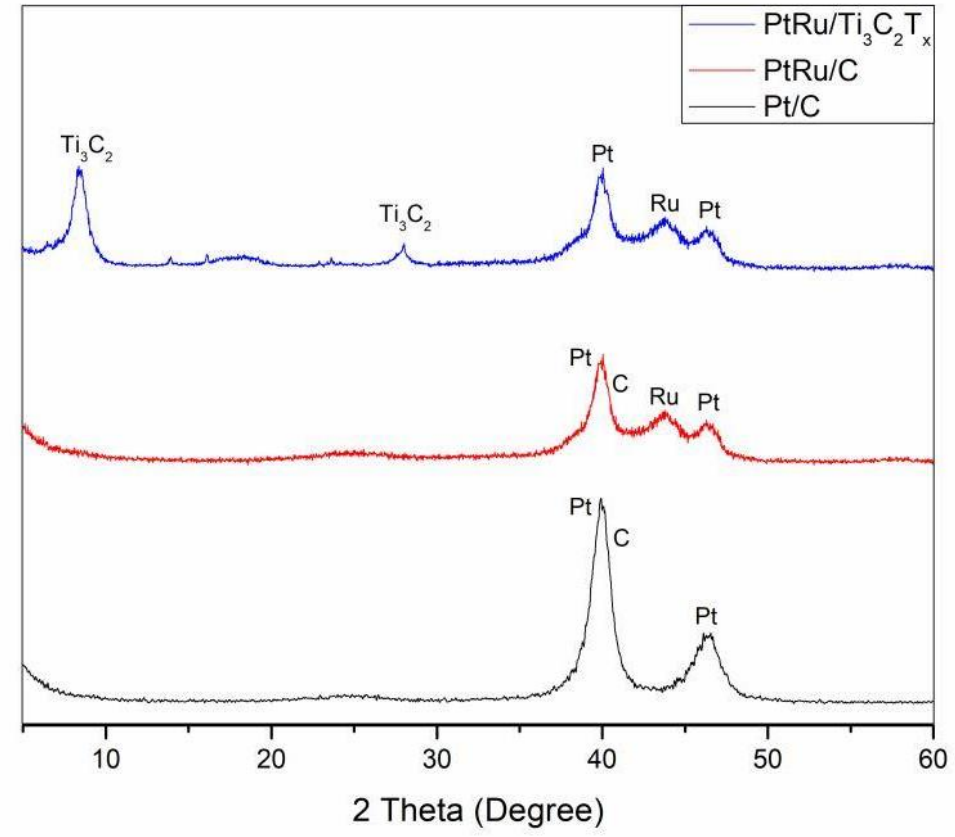

Figure 3: XRD pattern for $PtRu/Ti_3C_2T_x$, PtRu/C, and Pt/C electrocatalysts.

Table 1: The data of crystallite size for all elements present in the electrocatalysts.

Sample	**Crystallite Size (nm)**			
	Pt	**Ru**	**Ti_3C_2**	**C**
$PtRu/Ti_3C_2T_x$	10.14	15.62	9.17	–
PtRu/C	9.84	16.17	–	10.68
Pt/C	7.48	–	–	12.71

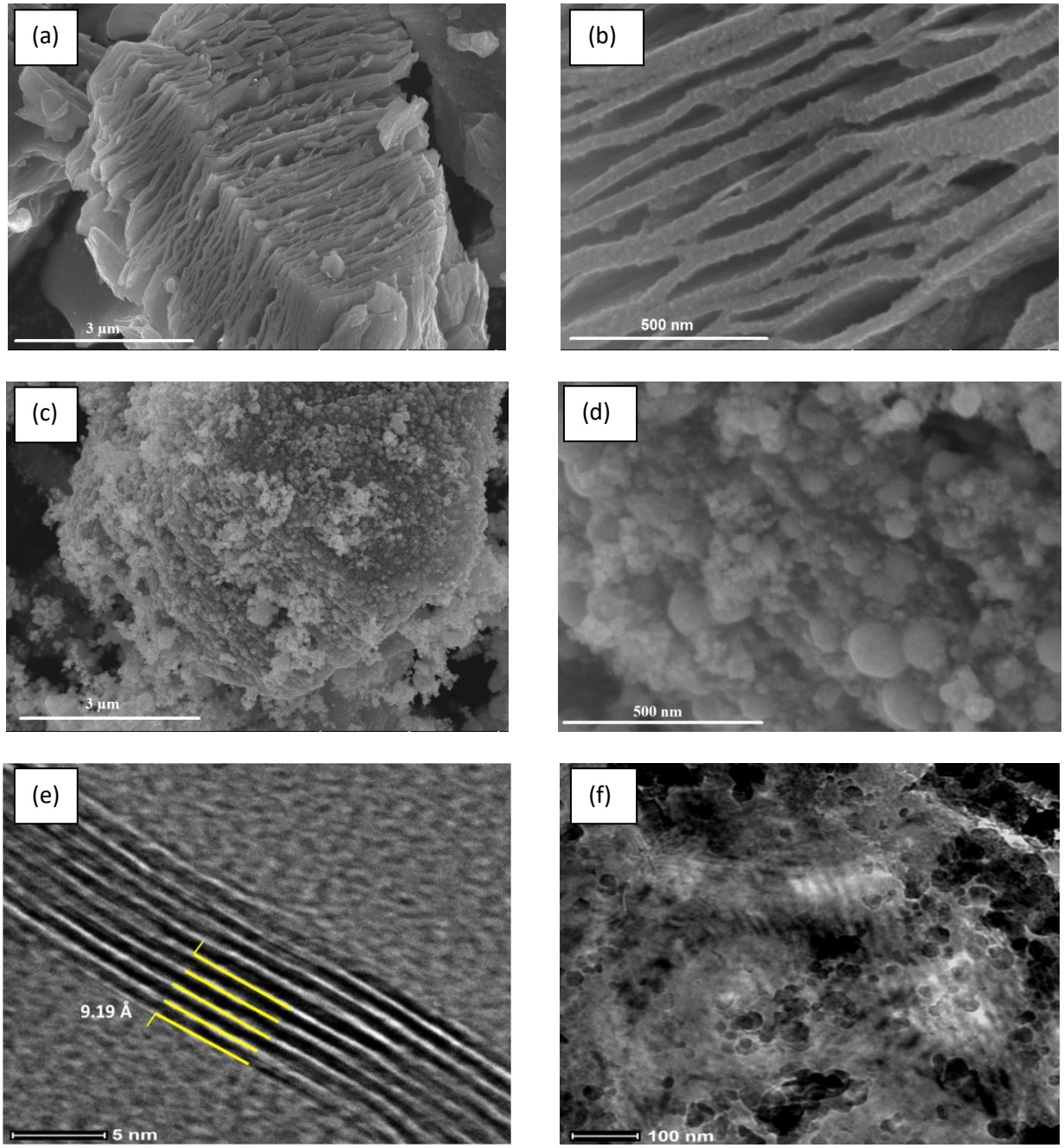

Figure 4: FESEM image for (a) $Ti_3C_2T_x$ catalyst support at low magnification, (b) $Ti_3C_2T_x$ catalyst support at high magnification, (c) PtRu/$Ti_3C_2T_x$ electrocatalyst at low magnification, (d) PtRu/$Ti_3C_2T_x$ electrocatalyst at high magnification; and TEM image for (e) $Ti_3C_2T_x$ catalyst support, (f) PtRu/$Ti_3C_2T_x$ electrocatalyst.

Surface morphology of the as-synthesized catalyst support and electrocatalyst, $Ti_3C_2T_x$ and PtRu/$Ti_3C_2T_x$, respectively, was investigated using FESEM and TEM analysis. Figure 4 (a) and (b) show the FESEM image of $Ti_3C_2T_x$ as a catalyst support at 15 kX and 100 kX magnification. The overall image spots the material with flaky and layered structure like a "wet book sheet". This kind of structure is the real structure of 2D MXene as agreed by other studies [36, 41] and indicates that the catalyst support is well synthesized. The FESEM image of PtRu/$Ti_3C_2T_x$ electrocatalyst is depicted in Figure 4 (c) and (d) at magnification of 15 kX and 100 kX. The image shows that the MXene structure is covered by a bundle of nanoparticles, namely, Pt and Ru. Roughly, the distribution of nanoparticles can be regarded as semi-uniform. However, the detailed material distribution was determined using SEM and mapping analysis. Figures 4 (e) and (f) present the detailed TEM image of $Ti_3C_2T_x$ catalyst support and PtRu/$Ti_3C_2T_x$ at scale of 5 nm and 100 nm, respectively. The TEM image of catalyst support illustrates the multilayer structure of 2D MXene with almost 10 layers. The average interlayer spacing of catalyst structure is 9.19 Å (0.919 nm), which is approximately the same as the expected value from the XRD analysis. Meanwhile, the TEM image of as-synthesized electrocatalyst shows the existence of other elements, Pt and Ru, on top of the $Ti_3C_2T_x$ catalyst support. The nanoparticles with smaller size are referred to as Pt, while those with larger size as Ru. The material distribution is investigated by mapping analysis. Figure 5 (a) show the SEM image of PtRu/$Ti_3C_2T_x$ electrocatalyst with wider view at magnification 4kX. The elemental mapping were analyzed based on SEM image from Figure 5 (a), and it is depicted in Figures 5 (b) – (d) for Pt, Ru, and Ti elements. The latter most elements represents the whole element of $Ti_3C_2T_x$ catalyst support, since the Ti and C elements are placed on the same distribution spot and pattern. The mapping images show that the Pt and Ru nanoparticles are adequately and

evenly distributed on the catalyst support owing to successful chemical reduction method during electrocatalyst synthesis process. At the same time, this situation shows a good sign for a good catalytic activity during MOR because of the increment of reaction surface area on the electrocatalyst.

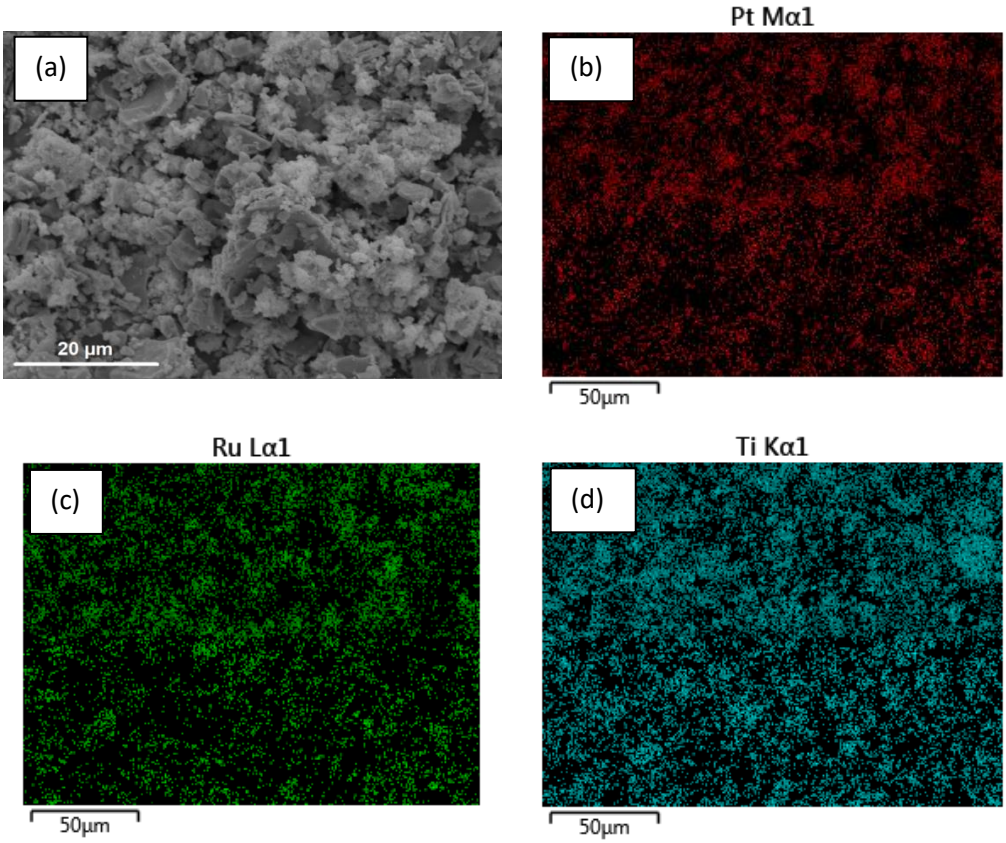

Figure 5: (a) SEM image of PtRu/$Ti_3C_2T_x$ electrocatalyst; (b) – (d) Mapping image for each element involved (Pt, Ru, Ti).

XPS analysis was conducted on the as-synthesized electrocatalyst, PtRu/$Ti_3C_2T_x$ to further understand the chemical state and chemical bonding at the electrocatalyst surface. The XPS spectra of the PtRu/$Ti_3C_2T_x$ electrocatalyst are shown in Figure 6. As can be seen, the spectra have shown the presence of Pt, Ru, Ti, and C elements in the electrocatalyst sample as discussed in the XRD and EDX analysis. Figure 6 (a) is the XPS survey spectra, while Figure 6

(b) – (e) are high-resolution XPS spectra for C 1s, Ru 3d, Pt 4f, Ti 2p and O 1s, respectively. Since the spectrum for C 1s and Ru 3d is overlapping, they are deconvulated simultaneously. The C 1s and Ru 3d spectra show the six peaks, where each three of them is fitted for each C 1s and Ru 3d element. The analysis results of the C 1s high-resolution spectra are located at 281.1 eV, 284.76 eV and 284.8 eV which indicate the presence of C-Ti-T_x and C-C bonds. The high-resolution spectra of Ti 2p show two main peaks that correspond to the C-Ti-OH bond (458.4 eV) and TiO_{2-x}-F_x (462.1 eV), while the O 1s spectra have two peaks at the binding energy of 529.7 eV and 531.0 eV which is the bonding of Ti-O_x and C-Ti-$(OH)_x$. With these three elements, it can be confirmed that a few peaks corresponding to $Ti_3C_2T_x$ elements have been formed, and several surface termination groups also can be seen on this material, including oxide (–O–), hydroxyl (–OH) and fluoride (–F) which formed during the etching process. The diagram for the high-resolution spectra for Pt 4f shows the appearance of four peaks involving the presence of metallic Pt (70.9 eV and 71.7 eV), PtO (74.2 eV) and $PtCl_x$ (75.2 eV), while the peaks for the Ru 3d spectra are at 279.7 eV and 280.3 eV, and 284.0 eV involving the presence of metallic Ru and RuO_x. The presence of oxide elements can also be seen in the Pt and Ru spectra that occur during the catalyst reduction process. The appearance of chloride bonds on the Pt element is caused by the incomplete reduction process from H_2PtCl_6 to Pt. However, this binding energy graph is the least prominent, which is only around 10%. The results of this analysis also show the presence of Pt and Ru in metal form, however, the alloy formation between these two elements cannot be analyzed in detail and it is highly suggested to further investigate this formation in future since the determination of alloy structure is essential for the catalytic behaviour and performance. The binding energy for each element is in line with several previous XPS studies involving $Ti_3C_2T_x$, Pt and Ru materials [42-45].

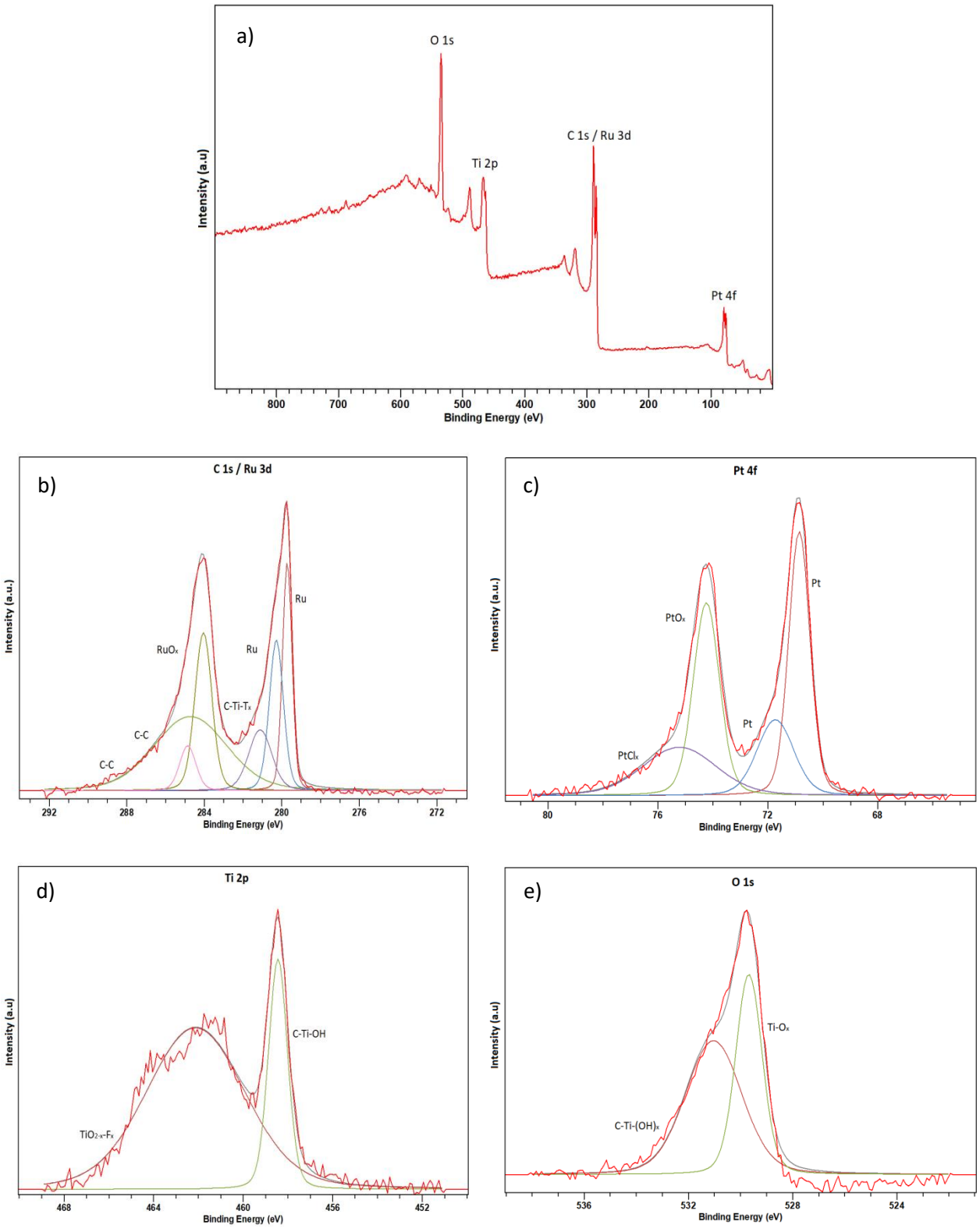

Figure 6: XPS analysis of PtRu/$Ti_3C_2T_x$ (a) XPS survey spectra; High resolution spectra of (b) Ti 2p, (c) O 1s, (d) C 1s and Ru 3d, and (e) Pt 4f.

3.2 Electrochemical Measurement of Electrocatalysts

Electrochemical performances of all electrocatalysts for MOR activity were measured using a half-cell. The CV profiles for all electrocatalysts are shown in Figure 7 (a), and data have been presented in Table 2. The active surface area is located in the hydrogen adsorption–desorption region at potential range of - 0.2 to 0.1 V versus Ag/AgCl. At this region, the adsorption-limited charge-transfer reaction takes place at the activation site, and the overall charge required for the adsorption/desorption of monolayer is used as ECSA active surface sites [46]. This ECSA value is an important parameter for electrocatalyst and represents the electrochemically accessible surface area [47] and catalyst utilization [46]. The ECSA results show that the as-synthesized electrocatalyst, PtRu/$Ti_3C_2T_x$, produced highest value of ECSA (55 $m^2\ g_{Pt}^{-1}$), followed by PtRu/C (37 $m^2\ g_{Pt}^{-1}$) and Pt/C (14 $m^2\ g_{Pt}^{-1}$) electrocatalysts. The ECSA value of PtRu/$Ti_3C_2T_x$ is almost 1.5 times higher than PtRu/C. This ECSA value is significantly higher compared with other previous studies conducted on 2D-materials composite as anodic electrocatalyst; Pt/$Ti_3C_2T_x$ [48], Pt/RGO [26], Pt/GNS [49] and PtMoS_2/RGO [50]. This is due to the unique structure of $Ti_3C_2T_x$ catalyst support in 2D dimension with opening layered structure, which gives the positive effect to the ECSA measurement. This structure allows more space for the PtRu bimetal catalyst to embed onto the catalyst support surface area. Therefore, it increases the catalyst utilization and reaction surface area and is anticipated to assist in better catalytic activity performance. This attachment of bimetal catalyst on the surface of catalyst support also guide toward strong catalyst–catalyst support reaction, which is one of the ideal characteristics to be an electrocatalyst.

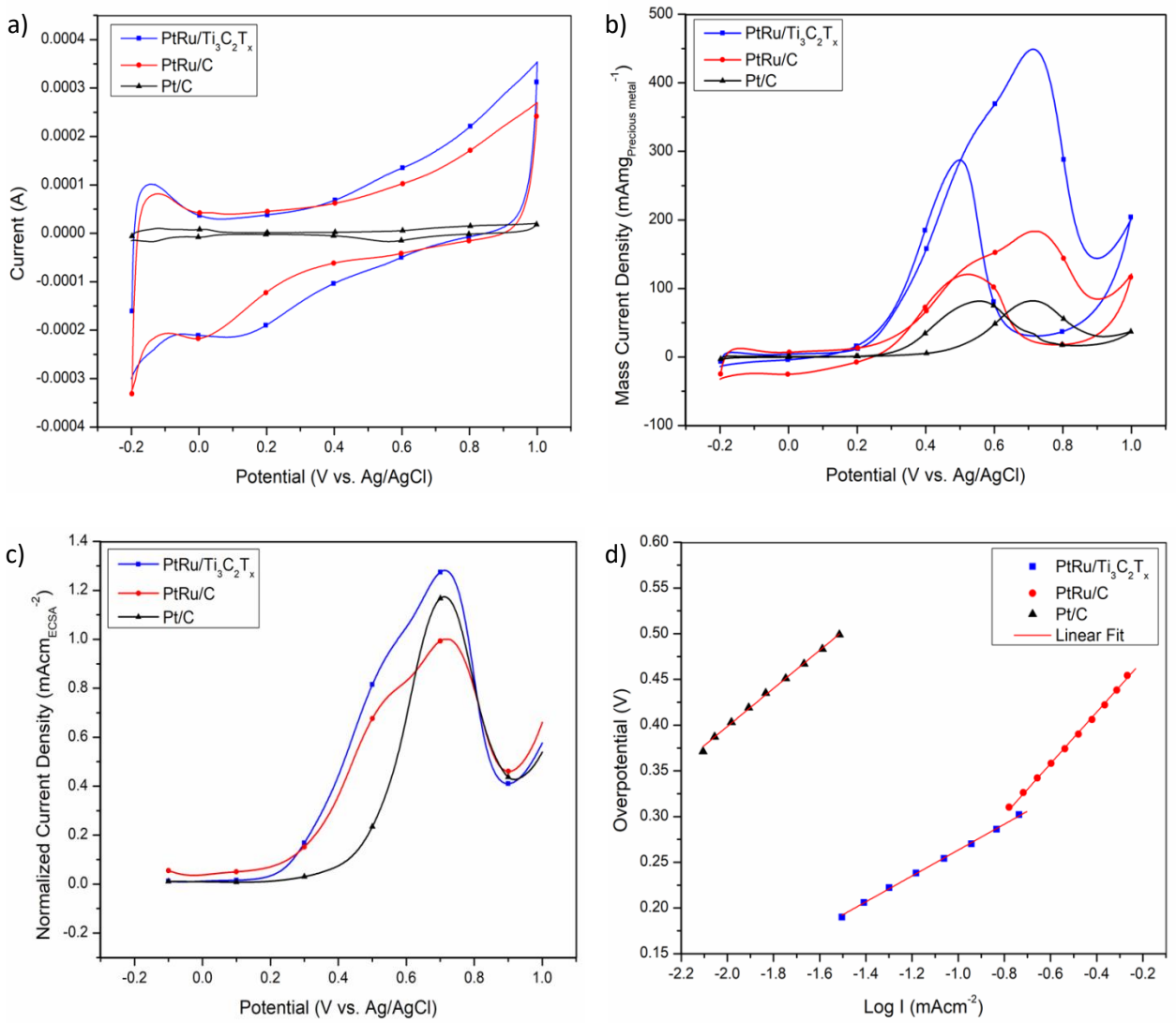

Figure 7: a) CV profile curve in 0.5 mol L^{-1} H_2SO_4 at scan rate of 20 mV s^{-1}, b) CV curve normalized by mass of precious metal, c) LSV curve normalized by ECSA in 2.8 mol L^{-1} CH_3OH and 0.5 mol L^{-1} H_2SO_4 at scan rate of 20 mV s^{-1}, and d) Tafel plot for $PtRu/Ti_3C_2T_x$, PtRu/C, and Pt/C electrocatalyst.

The electrocatalytic performance of all electrocatalysts for MOR was performed using CV measurement as depicted in Figures 7 (b). The CV curve was measured in the potential range of - 0.2 to 1.0 V versus Ag/AgCl, 0.5 mol L^{-1} of H_2SO_4 in 2.8 mol L^{-1} of CH_3OH, scan rate of 20 mV s^{-1}, with free-oxygen content, and at room temperature. The extraction data of CV curves are

summarized in Table 2. The results show that the as-synthesized electrocatalyst, PtRu/$Ti_3C_2T_x$, has the most negative curve, which demonstrate low onset potential value. This is a good sign for the electrocatalyst, because the more negative the value, the easier the removal of adsorbed CO intermediates on electrocatalyst surface [51]. This condition can boost the electrocatalytic activities during MOR.

Table 2: The extraction data from CV measurement for all electrocatalysts.

Electro-catalyst	**ECSA ($m^2 g_{Pt}^{-1}$)**	**Onset Potential (V versus Ag/AgCl)**	**Peak Potential (V versus Ag/AgCl)**	**Mass Current Density ($mA\ mg_{Precious\ metal}^{-1}$)**	**ECSA Current Density ($mA\ cm_{ECSA}^{-2}$)**	**CO Tolerance**
PtRu/$Ti_3C_2T_x$	55	0.29	0.71	449	1.36	1.56
PtRu/C	37	0.32	0.72	183	1.00	1.52
Pt/C	14	0.40	0.71	82	1.17	1.01

The CV curves in Figure 7 (b) show the peak current density normalized by the mass of precious metal, which indicate the mass of PtRu and Pt. These peak current density values indicate the catalytic activity of the electrocatalyst for MOR [52, 53]. The evaluation of peak current density is based on the highest peak attained during forward scan, which is between the potential ranges of 0.71 to 0.72 V versus Ag/AgCl. The results show that the mass peak current density of PtRu/$Ti_3C_2T_x$, generates the highest value, which is approximately 2.5 times higher than PtRu/C and 5.5 times higher than Pt/C. The high current density referred to the high electrocatalytic activity that can be produced by the anodic electrocatalyst in MOR. This situation occurred because of the existence of $Ti_3C_2T_x$ as one of the composite elements in the

electrocatalyst. $Ti_3C_2T_x$ is known for its 2D structure, which has unique properties that can help enhance the electrocatalytic activity by providing fast ion/charge transfer path [54]. This property is highly beneficial for the surface chemical reaction in electrocatalysis. The small crystallite size with high ECSA value by PtRu/$Ti_3C_2T_x$ electrocatalyst is also one of the main factors contributing to high electrocatalytic activity in MOR. Besides, $Ti_3C_2T_x$ is one of the highly active materials [54], allowing charge carriers to stimulate further into the catalyst support cluster, and strengthening the interaction between the catalyst support and metal catalyst, which contributes to the increase of reaction activity. All these factors enable the electrocatalysts with 2D structure materials to produce high electrocatalytic activity. The results indicate that the $Ti_3C_2T_x$ catalyst support can be a better substitute to pure carbon catalyst support (Vulcan XC-72R), which is commercially employed in DMFC technology.

The second highest mass current density was produced by the PtRu/C, followed by Pt/C electrocatalyst. These results are comparable to the results of studies conducted by several other researchers [55-57], who found that the use of Pt metal alone is unable to maximize the electrocatalytic activity. This is because the presence of other metals such as Ru can overcome the shortcomings of the Pt metal. The Ru metal in these electrocatalysts plays a vital role in reducing catalyst poisoning, by weakening the CO bond intensity, which causes CO adsorption to decrease. This is proven by CO tolerance data as shown in Table 2. The CO tolerance is calculated as the ratio of forward (I_f) and backward (I_b) oxidation peak. The backward oxidation peak emerges between 0.50 – 0.57 V versus Ag/AgCl owing to the incomplete formation of carbonaceous species at the forward oxidation peak. This oxidation involves the presence of CO, which is the main cause of catalyst poisoning in MOR. The CO tolerance results indicate that both electrocatalysts that used bimetal PtRu, PtRu/$Ti_3C_2T_x$ and PtRu/C produce much higher CO

tolerances than Pt/C. Between these two electrocatalysts, PtRu/$Ti_3C_2T_x$ has higher tolerance for carbonaceous species, with a ratio of 1.56, driven by maximizing the consumption of Ru at high electrocatalyst active surface area. These results also confirm that the combination of PtRu bimetal and $Ti_3C_2T_x$ 2D structure in the electrocatalyst can reduce catalyst poisoning problems faced by DMFC technology. The peak current density of PtRu/$Ti_3C_2T_x$ electrocatalyst is comparable and higher than other several studies conducted recently on $Ti_3C_2T_x$–based electrocatalyst for methanol oxidation. Pd/$Ti_3C_2T_x$ [31], MoS_2QDs@$Ti_3C_2T_x$QDs@MWCNTs [34], Pt-MXene-TiO_2[58], Pt/$(Ti_3C_2T_x)_{0.5}$-$(MWCNTs)_{0.5}$[59], Pt NW/PDDA-$Ti_3C_2T_x$ [60] are the relevant studies conducted by other researchers.

LSV is one of the main approaches for measuring the electrocatalytic activity, and this LSV data is normalized with ECSA value to explore the intrinsic activity of the electrocatalyst [61-62]. Figure 7 (c) displays the curve of ECSA-normalized peak current density for all electrocatalysts. The graph clearly shows that the as-synthesized electrocatalyst, PtRu/$Ti_3C_2T_x$, has the highest peak current density value compared with other electrocatalyst after ECSA normalization. This indicate that the PtRu/$Ti_3C_2T_x$ electrocatalyst has a higher intrinsic activity than PtRu/C and Pt/C in MOR, which can assume that there are more exposed catalytically active sites and can achieve better mass transport during the reaction [63]. This situation leads to the better catalytic performance as achieved in CV results. The data from this LSV measurement are employed in Tafel analysis. In the LSV curve, the Tafel region occurs around potential range of 0.19 to 0.5 V versus Ag/AgCl and the Tafel plot is shown in Figure 7 (d), while the extracted data of Tafel analysis is summarized in Table 3.

Table 3: The Tafel analysis data for PtRu/$Ti_3C_2T_x$, PtRu/C, and Pt/C electrocatalysts.

Electrocatalyst	**Tafel Slope, *b* (mV dec^{-1})**	**Ion Exchange Current Density, *a* (mA cm^{-2})**	**Charge Transfer Coefficient, *α***	**Standard Deviation, R^2**
PtRu/$Ti_3C_2T_x$	146	0.41	0.41	0.99
PtRu/C	275	0.52	0.22	0.99
Pt/C	208	0.82	0.28	0.99

The results show that Tafel slope for all the electrocatalysts lies in the range of 146 to 275 mV dec^{-1}, which is equal to the methanol decomposition span for Pt-based electrocatalyst, which lies in the range of 95 to 440 mV dec^{-1} [64]. This indicates that the methanol decomposition is adequate for all electrocatalysts. Figure 7 (d) showed that the as-synthesized electrocatalyst, PtRu/$Ti_3C_2T_x$, has the lowest overpotential compared with other electrocatalysts, suggesting the intrinsic optimization of electrochemical active sites [65]. The Tafel slope for all electrocatalysts in increasing order is as follows: PtRu/$Ti_3C_2T_x$< Pt/C <PtRu/C. The smaller the Tafel slope the faster the kinetic reaction activity. These results show that the PtRu/$Ti_3C_2T_x$ electrocatalyst involves the fastest reaction and superior catalytic activity among all electrocatalysts. The higher reaction activity can be attributed to the existence of Pt and Ru nanoparticles on the top of the electrocatalyst surface as evidenced in the SEM and TEM image. Small nanoparticles facilitate transportation of ion into the reaction spot of methanol adsorption, thereby accelerating the MOR [66].

Table 3 also shows that the ion exchange current densities for all electrocatalyst, and Pt/C has a high value of current density, i.e., 0.82 mA cm^{-2}. This indicates that Pt/C can produce the best catalytic activity compared with other electrocatalysts [67]. However, the low value of ECSA, CO tolerance, and Tafel slope, as well as high onset potential makes it impossible to

yield a high performance for DMFC. This result proved that the catalyst poisoning and slow reaction kinetics become the main obstacles for this electrocatalyst to be employed as commercial electrocatalyst in MOR. The charge-transfer coefficient is one of the important values in electrochemical study, where it describes the properties of electron transfer in reaction. Table 3 shows the charge-transfer coefficients for all electrocatalysts in the range of 0.22 – 0.41. It can be stated that reactions are related to CH_3OH dissociation with value close to $\pm$ 0.5 but greater than 0 [64]. This means that all electrocatalysts undergo two main reactions involving O–H and C–H bond breaking with unconventional charge-transfer coefficient value at solid–liquid interface. The presence of this unconventional value is associated with a dramatic structure change of solvation shell from initial state to transition state [64].

Table 4: Comparison of current density value of $PtRu/Ti_3C_2T_x$ electrocatalyst with previous studies.

Authors	**Electrocatalysts**	**Mass Current Density ($mA\ mg_{Precious\ metal}^{-1}$)**	**Geometric Current Density ($mA\ cm_{Geo}^{-2}$)**	**ECSA Current Density ($mA\ cm_{ECSA}^{-2}$)**
This study	$PtRu/Ti_3C_2T_x$	449	38	1.36
Ramirez et al. [68]	Pt/FAU-C	-	12	-
Patil et al. [49]	Pt/MoS_2	177.4	3.07	-
Shahrokhian et al. [69]	PtPd-NFs/rGO	-	-	1.15
Sha et al. [70]	PtNFs/rGO	-	15.3	-
Wang et al. [71]	Pt/Co-PC	295.4	-	-
Kumar et al. [72]	PtPd/rGO	-	-	0.49

Table 4 presents the comparison between the current density values of PtRu/$Ti_3C_2T_x$ electrocatalyst with previous studies on Pt-based electrocatalyst in acidic medium solution for methanol oxidation process. The comparison reveals that PtRu/$Ti_3C_2T_x$ has the highest peak value of current density among all the Pt-based electrocatalysts under similar experimental conditions. In addition, the ECSA normalized-current density for PtRu/$Ti_3C_2T_x$ also possess highest value compare to other two electrocatalyst by Shahrokhian et al. [69] and Kumar et al. [72], which showed that the as-synthesized electrocatalyst not only have high peak current density, but also an intrinsically active material for MOR. This result shows that the $Ti_3C_2T_x$ 2D material plays a critical role in enhancing electrocatalytic activity.

Further exploration on interface electrical resistance of the material for all electrocatalysts was conducted using EIS measurement in galvanostatic mode. This mode of operation was performed to avoid the occurrence of simultaneous two-factor changes in the impedance measurement. The two factors are current and time, which change when the impedance measurement is carried out [73]. Thus, controlling one of the factors (i.e., current) can provide more accurate impedance measurement. The EIS measurement in galvanostatic mode controls the current at the electrode and at the same time forces a constant conversion rate with respect to the (charged) species involved in the electrode reaction [74]. Therefore, it is assumed that the impedance spectrum measurement in this mode of operation is dominated by the anodic half-cell reaction.

Figure 8 (a) shows the Nyquist plot for PtRu/$Ti_3C_2T_x$, PtRu/C, and Pt/C electrocatalysts in the sweeping frequency range of 100 kHz and 1 Hz, and 2.8 mol L^{-1} CH_3OH in 0.5 mol L^{-1} H_2SO_4 solution. The Nyquist plots for all electrocatalysts depict the same pattern with existence of a small semicircle and joint with a line. This semicircle arc occurs because of the charge-

transfer resistance of the interface material, while a straight line represents the diffusion limiting step during MOR [75]. The Nyquist plot of half-cell performance for methanol oxidation process was fitted using the Randles equivalent circuit model as illustrated in Figure 8 (b). The circuit consists of four components, namely, resistors (R_s and R_{ct}, which represent the resistance of solution or electrolyte and resistance of charge transfer), capacitance, constant phase element (CPE) and Warburg element. The result of the fitting process is tabulated in Table 5.

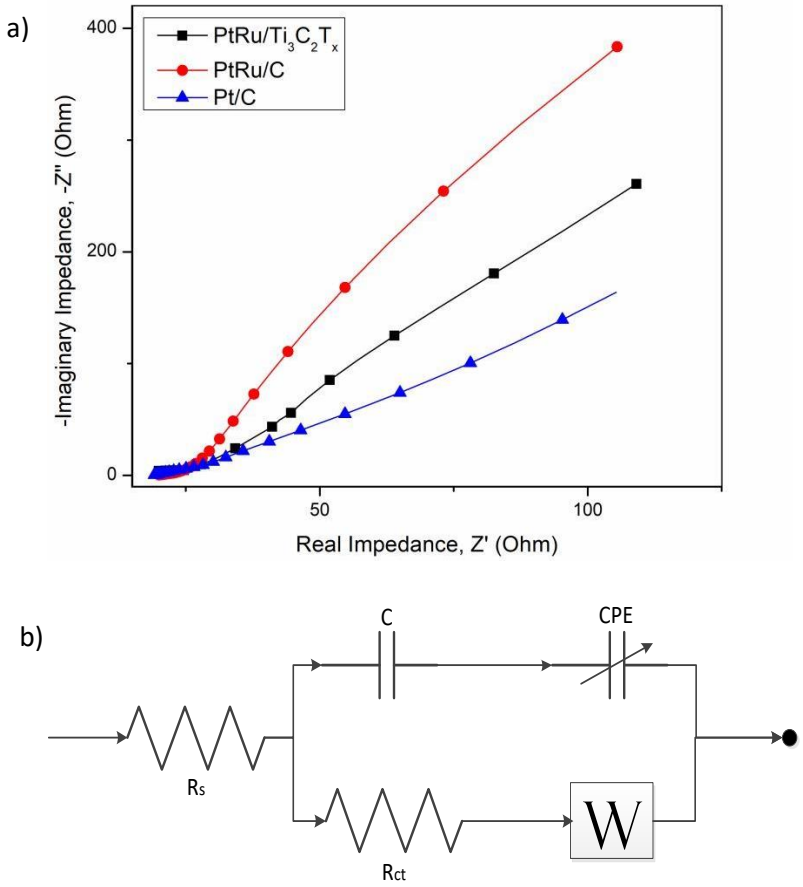

Figure 8: (a) Nyquist plot for MOR PtRu/$Ti_3C_2T_x$, PtRu/C and Pt/C electrocatalyst in 2.8 mol L^{-1} CH_3OH and 0.5 mol L^{-1} H_2SO_4 solution; and (b) equivalent circuit model for half-cell performance.

Table 5: EIS data from the fitting of equivalent circuit model for all electrocatalysts.

Electrocatalyst	**R_s (Ω cm^2)**	**R_{ct} (Ω cm^2)**	**W ($S\ s^{1/2}$)**	**Goodness of Fit (%)**
PtRu/$Ti_3C_2T_x$	1.32	2.66	$238x10^{-6}$	1.70
PtRu/C	1.33	4.22	$259x10^{-6}$	1.52
Pt/C	1.32	5.60	$49x10^{-6}$	1.12

The Nyquist plot shows that the PtRu/$Ti_3C_2T_x$ electrocatalyst has the smallest semicircle diameter compared with other electrocatalyst, which explains the great charge transport performance towing to small interface electrical resistance of the material [76]. The results on EIS data table show that the R_s value for all electrocatalysts is almost the same as the same electrolyte was consumed for the measurement. Furthermore, the value of R_{ct} in increasing order for all electrocatalysts is as follows: PtRu/$Ti_3C_2T_x$<PtRu/C <Pt/C. The R_{ct} value for $Ti_3C_2T_x$-composite is smaller than carbon-composite electrocatalyst is matched with other previous study by Wang et al. [33] and Yang et al. [60]. This indicates that the $Ti_3C_2T_x$-composite electrocatalyst has the smallest charge-transfer resistance at the material interface and increases the chemical absorption efficiency of methanol in the catalyst area; it thus helps improve the electrocatalytic activity and MOR performance. This result also reveals that the PtRu/$Ti_3C_2T_x$ has high electron conductivity compared with PtRu/C and PtC electrocatalysts [77]. The straight line at low frequency in the Nyquist plot denotes the existence of Warburg element in the equivalent circuit. The result shows that the PtRu/C and PtRu/$Ti_3C_2T_x$ has high value of Warburg impedance (denoted as W in Table 5), which indicates a better diffusion of methanol for the electrocatalyst [78]. Therefore, the as-synthesized electrocatalyst, PtRu/$Ti_3C_2T_x$, has better resistance, high chemical absorption and electron conductivity, and good diffusion of methanol

for MOR compared with PtRu/C and Pt/C. This result describes the excellent electrocatalytic activity as acquired during CV measurement.

3.3 Single-Cell Performance

The electrocatalysts, PtRu/$Ti_3C_2T_x$, PtRu/C, and Pt/C were tested for DMFC single-cell performance. A total of 4 cm^2 active surface area of anode electrode was flanked by membrane and cathode electrode, which transformed as MEA for single-cell performance testing using 2.8 mol L^{-1} CH_3OH in passive system conditions. Figure 9 shows the current–voltage (I–V) curves for all electrocatalysts, where the left and right arrows show respectively the graph of voltage and power density versus current density. The maximum power density values of as-synthesized electrocatalyst show approximately 56 % and 70 % increment compared with the PtRu/C and Pt/C electrocatalysts, respectively. Maximum power density values for PtRu/$Ti_3C_2T_x$, PtRu/C, and Pt/C are 3.43, 2.20, and 2.02 mW cm^{-2}, respectively.

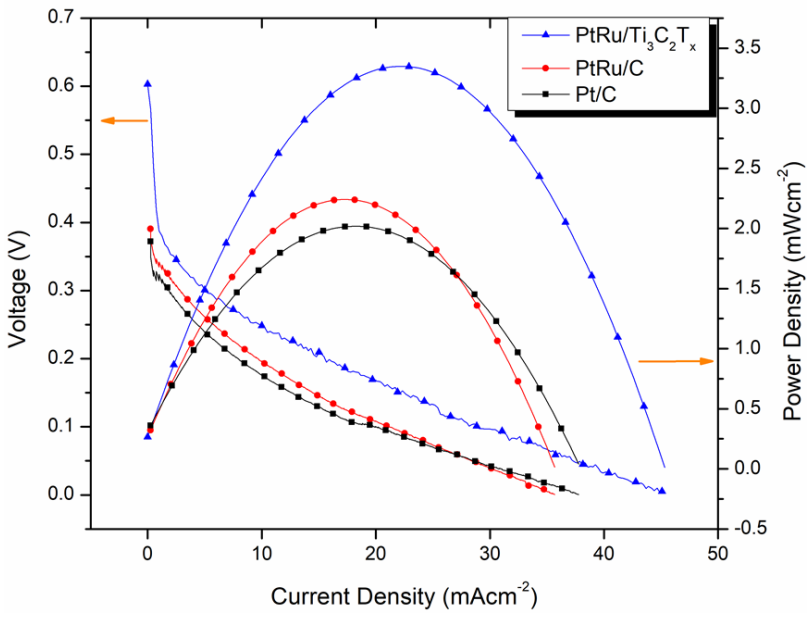

Figure 9: Current–Voltage (I–V) curves for PtRu/$Ti_3C_2T_x$, PtRu/C, and Pt/C by using 2.8 mol L^{-1} CH_3OH at room temperature.

This increment shown by PtRu/$Ti_3C_2T_x$ electrocatalyst is because of the good physical and electrochemical properties of electrocatalyst. The unique structure of $Ti_3C_2T_x$ 2D material opens up more space for Pt Ru bimetal to attach and distribute well on the catalyst support, thereby increasing the catalyst–catalyst support interaction. Other than that, the PtRu/$Ti_3C_2T_x$ electrocatalyst also has highly exposed catalytic active sites and better mass transport resulting in higher intrinsic activity during MOR. The better result for as-synthesized electrocatalyst is also due to the high catalytic activity, high tolerance toward poisonous species, fast kinetic reaction, and low charge-transfer resistance. The overall electrochemical performance and single-cell measurements confirm that the combination of bimetal catalysts PtRu and the introduction of 2D structured materials have a high potential to replace Pt/C electrocatalyst in DMFC technology. This study also proved that the $Ti_3C_2T_x$ 2D material has assisted the electrocatalyst to achieve high performance in the electrochemical reaction, which is also expected to be suitable for used as a material in other types of electrochemical energy conversion systems and further study is recommended in future.

4.0 CONCLUSIONS

In this study, the PtRu bimetal was reduced to the $Ti_3C_2T_x$ 2D material via chemical reduction method. This electrocatalyst is introduced as a new formulation of anodic electrocatalyst for DMFC application. The PtRu/$Ti_3C_2T_x$ electrocatalyst was compared with two other electrocatalysts, namely, PtRu/C and Pt/C, to examine the effect of $Ti_3C_2T_x$ and Ru element on MOR. All electrocatalysts underwent several physical characterizations, electrochemical measurements, and single-cell performance tests. The XRD patterns and XPS spectra reveal the presence of all elements (Pt, Ru, Ti_3C_2, and C) in the electrocatalyst sample. Meanwhile, the

SEM, TEM, and mapping image portray the flaky 2D structure of $Ti_3C_2T_x$ and adequate distribution of PtRu bimetal on the surface of $Ti_3C_2T_x$. The electrochemical measurement revealed high electrochemical surface area (55 $m^2 g^{-1}$), high electrocatalytic and intrinsic activity (449 mA mg_{PtRu}^{-1}/ 1.36 mA cm_{ECSA}^{-2}), high resistance toward carbonaceous intermediate species, more negative onset potential, and fast kinetic reaction compared with other electrocatalyst. Besides, the EIS measurement shows that PtRu/$Ti_3C_2T_x$ electrocatalyst exhibits smallest charge-transfer resistance. The electrochemical measurements data show a good sign for PtRu/$Ti_3C_2T_x$ electrocatalyst to be an ideal anodic electrocatalyst for MOR. To validate the data, the electrocatalyst was applied in the DMFC single cell system with 4 cm^2 active surface area. The I – V curve shows that PtRu/$Ti_3C_2T_x$ electrocatalyst has highest power density, which is approximately 70 % increment compared with Pt/C electrocatalyst. This result shows that PtRu/$Ti_3C_2T_x$ electrocatalyst has good electrochemical properties, high single-cell performance, and can be a promising anodic electrocatalyst for DMFC application.

ACKNOWLEDGEMENT

Authors would like to acknowledge the financial support provided by the Sunway University through the project no #STR-RCGS-MATSCI[S]-001-2021.

CONFLICT OF INTEREST

We confirm that this manuscript is original, has not been published elsewhere and not under consideration for publication elsewhere. This manuscript also has been approved by all co-authors. The authors declare that they have no conflicts of interest to disclose.

REFERENCES

1. Lucia, U., Overview on fuel cells. Renewable Sustainable Energy Reviews, 2014. **30**: p. 164-169.
2. Abdullah, N. and S. Kamarudin, Titanium dioxide in fuel cell technology: an overview. Journal of Power Sources, 2015. **278**: p. 109-118.
3. Ramli, Z. and S. Kamarudin, Platinum-based catalysts on various carbon supports and conducting polymers for direct methanol fuel cell applications: a review. Nanoscale research letters, 2018. **13**(1): p. 410.
4. Giorgi, L. and F. Leccese, Fuel cells: technologies and applications. The Open Fuel Cells Journal, 2013. **6**(1).
5. Kamarudin, S.K., F. Achmad, and W.R.W. Daud, Overview on the application of direct methanol fuel cell (DMFC) for portable electronic devices. International Journal of hydrogen energy, 2009. **34**(16): p. 6902-6916.
6. Mallakpour, S., et al., Improving the direct methanol fuel cell performance with poly (vinyl alcohol)/titanium dioxide nanocomposites as a novel electrolyte additive. International Journal of Hydrogen Energy, 2013. **38**(28): p. 12418-12426.
7. Sharaf, O.Z. and M.F. Orhan, An overview of fuel cell technology: Fundamentals and applications. Renewable Sustainable Energy Reviews, 2014. **32**: p. 810-853.
8. Olabi, A., Renewable energy and energy storage systems. Energy, 2017. **136**: p. 1-6.
9. Baldauf, M. and W. Preidel, Status of the development of a direct methanol fuel cell. Journal of Power Sources, 1999. **84**(2): p. 161-166.

10. Siwal, S.S., S. Thakur, Q.B. Zhang and V.K. Thakur, Electrocatalysts for electrooxidation of direct alcohol fuel cell: Chemistry and applications. Materials Today Chemistry, 2019. **14**: p. 100182.
11. Samimi, F. and M.R. Rahimpour, Direct methanol fuel cell, in Methanol. 2018, Elsevier. p. 381-397.
12. Joghee, P., J.N. Malik, S. Pylypenko, and R. O'Hayre, A review on direct methanol fuel cells–In the perspective of energy and sustainability. MRS Energy Sustainability, 2015. **2**.
13. McNicol, B., D.A. Rand, and K. Williams, Fuel cells for road transportation purposes—yes or no?. Journal of Power Sources, 2001. **100**(1-2): p. 47-59.
14. Munjewar, S.S., S.B. Thombre, and R.K. Mallick, Approaches to overcome the barrier issues of passive direct methanol fuel cell–Review. Renewable Sustainable Energy Reviews, 2017. **67**: p. 1087-1104.
15. Abdullah, M., S. Kamarudin, and L. Shyuan, TiO2 nanotube-carbon (TNT-C) as support for Pt-based catalyst for high methanol oxidation reaction in direct methanol fuel cell. Nanoscale research letters, 2016. **11**(1): p. 553.
16. Abdullah, N., S.K. Kamarudin, L.K. Shyuan and N.A. Karim, Synthesis and optimization of PtRu/TiO2-CNF anodic catalyst for direct methanol fuel cell. International Journal of Hydrogen Energy, 2019. **44**(58): p. 30543-30552.
17. Amani, M., M. Kazemeini, M. Hamedanian, H. Pahlavanzadeh and H. Gharibi, Investigation of methanol oxidation on a highly active and stable Pt–Sn electrocatalyst supported on carbon–polyaniline composite for application in a passive direct methanol fuel cell. Materials Research Bulletin, 2015. **68**: p. 166-178.

18. Ercelik, M., A. Ozden, E. Seker and C.O. Colpan, Characterization and performance evaluation of PtRu/CTiO2 anode electrocatalyst for DMFC applications. International Journal of Hydrogen Energy, 2017. **42**(33): p. 21518-21529.
19. Zheng, Y., Z. Zhang, X. Zhang, H. Ni, Y. Sun, Y. Lou, X. Li and Y. Lu, Application of Pt-Co nanoparticles supported on CeO2-C as electrocatalyst for direct methanol fuel cell. Materials Letters, 2018. **221**: p. 301-304.
20. Munjewar, S.S., S.B. Thombre, and R.K. Mallick, A comprehensive review on recent material development of passive direct methanol fuel cell. Ionics, 2017. **23**(1): p. 1-18.
21. Mansor, M., S.N. Timmiati, K.L. Lim, W.Y. Wong, S.K. Kamarudin and N.H.N. Kamarudin, Recent progress of anode catalysts and their support materials for methanol electrooxidation reaction. International Journal of Hydrogen Energy, 2019. **44**(29): p. 14744-14769.
22. Iqbal, M.Z., A.-U. Rehman, and S. Siddique, Prospects and challenges of graphene based fuel cells. Journal of Energy Chemistry, 2019. **39**: p. 217-234.
23. Wang, Z., H. Gao, Q. Zhang, Y. Liu, J. Chen, and Z. Guo, Recent advances in 3D graphene architectures and their composites for energy storage applications. Small, 2019. **15**(3): p. 1803858.
24. Su, H. and Y.H. Hu, Recent advances in graphene-based materials for fuel cell applications. Energy Science Engineering, 2021. **9**(7): p. 958-983.
25. Zhang, Q., Y. Li, T. Chen, L. Li, S. Shi, C. Jin, B. Yang, and S. Hou, Fabrication of 3D interconnected porous MXene-based PtNPs as highly efficient electrocatalysts for methanol oxidation. Journal of Electroanalytical Chemistry, 2021. **894**: p. 115338.

26. Yang, C., Q. Jiang, W. Li, H. He, L. Yang, Z. Lu, and H. Huang, Ultrafine Pt nanoparticle-decorated 3D hybrid architectures built from reduced graphene oxide and MXene nanosheets for methanol oxidation. Chemistry of Materials, 2019. **31**(22): p. 9277-9287.
27. Lei, J.-C., X. Zhang, and Z. Zhou, Recent advances in MXene: Preparation, properties, and applications. Frontiers of Physics, 2015. **10**(3): p. 276-286.
28. VahidMohammadi, A., J. Rosen, and Y. Gogotsi, The world of two-dimensional carbides and nitrides (MXenes). Science, 2021. **372**(6547): p. eabf1581.
29. Zhang, X., Z. Zhang, and Z. Zhou, MXene-based materials for electrochemical energy storage. Journal of Energy Chemistry, 2018. **27**(1): p. 73-85.
30. Askari, M.B., P. Salarizadeh, M. Seifi, and S.M. Rozati, Ni/NiO coated on multi-walled carbon nanotubes as a promising electrode for methanol electro-oxidation reaction in direct methanol fuel cell. Solid State Sciences, 2019. **97**: p. 106012.
31. Lang, Z., Z. Zhuang, S. Li, L. Xia, Y. Zhao, Y. Zhao, C. Han and L. Zhou, MXene surface terminations enable strong metal–support interactions for efficient methanol oxidation on palladium. ACS Applied Materials Interfaces, 2019. **12**(2): p. 2400-2406.
32. Kong, F., X. He, Q. Liu, X. Qi, Y. Zheng, R. Wang and Y. Bai, Improving the electrochemical properties of MXene Ti3C2 multilayer for Li-ion batteries by vacuum calcination. Electrochimica Acta, 2018. **265**: p. 140-150.
33. Wang, Y., J. Wang, G. Han, C. Du, Q. Deng, Y. Gao, G. Yin and Y. Song, Pt decorated Ti3C2 MXene for enhanced methanol oxidation reaction. Ceramics International, 2019. **45**(2): p. 2411-2417.
34. Yang, X., Q. Jia, F. Duan, B. Hu, M. Wang, L. He, Y. Song and Z. Zhang, Multiwall carbon nanotubes loaded with MoS2 quantum dots and MXene quantum dots: Non–Pt bifunctional

catalyst for the methanol oxidation and oxygen reduction reactions in alkaline solution. Applied Surface Science, 2019. **464**: p. 78-87.

35. Aslfattahi, N., R. Saidur, A. Arifutzzaman, R. Sadri, N. Bimbo, M.F.M. Sabri, P.A. Maughan, L. Bouscarrat, R.J. Dawson and S.M. Said, Experimental investigation of energy storage properties and thermal conductivity of a novel organic phase change material/MXene as A new class of nanocomposites. Journal of Energy Storage, 2020. **27**: p. 101115.
36. Abdullah, N., R. Saidur, A.M. Zainoodin and N. Aslfattahi, Optimization of electrocatalyst performance of platinum-ruthenium induced with MXene by response surface methodology for clean energy application. Journal of Cleaner Production, 2020: p. 123395.
37. Feng, A., Y. Yu, F. Jiang, Y. Wang, L. Mi, Y. Yu and L. Song, Fabrication and thermal stability of NH4HF2-etched Ti3C2 MXene. Ceramics International, 2017. **43**(8): p. 6322-6328.
38. Ma, Y., R. Wang, H. Wang, V. Linkov and S. Ji, Evolution of nanoscale amorphous, crystalline and phase-segregated PtNiP nanoparticles and their electrocatalytic effect on methanol oxidation reaction. Physical Chemistry Chemical Physics, 2014. **16**(8): p. 3593-3602.
39. Zhao, Y., J. Liu, C. Liu, F. Wang and Y. Song, Amorphous CuPt alloy nanotubes induced by Na2S2O3 as efficient catalysts for the methanol oxidation reaction. ACS Catalysis, 2016. **6**(7): p. 4127-4134.
40. Nkabinde, S.S., Z.B. Ndala, N.P. Shumbula, T. Kolokoto, O. Nchoe, G.N. Ngubeni, K.P. Mubiayi and N. Moloto, Delineating the role of crystallinity in the electrocatalytic activity of colloidally synthesized MoP nanocrystals. New Journal of Chemistry, 2020. **44**(33): p. 14041-14049.

41. Aslfattahi, N., L. Samylingam, A.S. Abdelrazik, A. Arifutzzaman and R. Saidur, MXene based new class of silicone oil nanofluids for the performance improvement of concentrated photovoltaic thermal collector. Solar Energy Materials and Solar Cells, 2020. **211**: p. 110526.
42. Shen, B., H. Huang, H. Liu, Q. Jiang, and H. He, Bottom-up construction of three-dimensional porous MXene/nitrogen-doped graphene architectures as efficient hydrogen evolution electrocatalysts. International Journal of Hydrogen Energy, 2021. **46**(58): p. 29984-29993.
43. Yang, C., H. He, Q. Jiang, X. Liu, S.P. Shah, H. Huang, and W. Li, Pd nanocrystals grown on MXene and reduced graphene oxide co-constructed three-dimensional nanoarchitectures for efficient formic acid oxidation reaction. International Journal of Hydrogen Energy, 2021. **46**(1): p. 589-598.
44. Kim, H.J., S.M. Choi, S. Green, G.A. Tompsett, S.H. Lee, G.W. Huber, and W.B. Kim, Highly active and stable PtRuSn/C catalyst for electrooxidations of ethylene glycol and glycerol. Applied Catalysis B: Environmental, 2011. **101**(3-4): p. 366-375.
45. Chastain, J. and R.C. King Jr, Handbook of X-ray photoelectron spectroscopy. Perkin-Elmer Corporation, 1992. **40**: p. 221.
46. Cooper, K.R., In situ PEM fuel cell electrochemical surface area and catalyst utilization measurement, in *Fuel Cell Magazine*. 2009.
47. Rudi, S., C. Cui, L. Gan, and P. Strasser, Comparative study of the electrocatalytically active surface areas (ECSAs) of Pt alloy nanoparticles evaluated by H upd and CO-stripping voltammetry. Electrocatalysis, 2014. **5**(4): p. 408-418.
48. Yang, C., Q. Jiang, H. Liu, L. Yang, H. He, H. Huang and W. Li, Pt-on-Pd bimetallic nanodendrites stereoassembled on MXene nanosheets for use as high-efficiency

electrocatalysts toward the methanol oxidation reaction. Journal of Materials Chemistry A, 2021. **9**(27): p. 15432-15440.

49. Patil, S.H., B. Anothumakkool, S.D. Sathaye and K.R. Patil, Architecturally designed Pt–MoS 2 and Pt–graphene composites for electrocatalytic methanol oxidation. Physical Chemistry Chemical Physics, 2015. **17**(39): p. 26101-26110.
50. Zhai, C., M. Zhu, D. Bin, F. Ren, C. Wang, P. Yang and Y. Du, Two dimensional MoS2/graphene composites as promising supports for Pt electrocatalysts towards methanol oxidation. Journal of Power Sources, 2015. **275**: p. 483-488.
51. Lu, S., H. Li, J. Sun and Z. Zhuang, Promoting the methanol oxidation catalytic activity by introducing surface nickel on platinum nanoparticles. Nano Research, 2018. 11(4): p. 2058-2068.
52. Siller-Ceniceros, A.A., M.E. Sánchez-Castro, D. Morales-Acosta, J.R. Torres-Lubian and F.J. Rodríguez-Varela, Innovative functionalization of Vulcan XC-72 with Ru organometallic complex: significant enhancement in catalytic activity of Pt/C electrocatalyst for the methanol oxidation reaction (MOR). Applied Catalysis B: Environmental, 2017. **209**: p. 455-467.
53. Zhao, S., H. Yin, L. Du, G. Yin, Z. Tang and S. Liu, Three dimensional N-doped graphene/PtRu nanoparticle hybrids as high performance anode for direct methanol fuel cells. Journal of Materials Chemistry A, 2014. **2**(11): p. 3719-3724.
54. Yuan, W. and L. Cheng, MXenes for Electrocatalysis. MXenes: Fundamentals applications. Vol. 51. 2019, Millersville, USA: Materials Research Forum LLC. 74-104.

55. Çögenli, M.S. and A.B. Yurtcan, Catalytic activity, stability and impedance behavior of PtRu/C, PtPd/C and PtSn/C bimetallic catalysts toward methanol and formic acid oxidation. International Journal of Hydrogen Energy, 2018. **43**(23): p. 10698-10709.
56. Tao, Z., W. Chen, J. Yang, X. Wang, Z. Tan, J. Ye, Y. Chen and Y. Zhu, Ultrathin yet transferrable Pt-or PtRu-decorated graphene films as efficient electrocatalyst for methanol oxidation reaction. Science China Materials, 2019. **62**(2): p. 273-282.
57. Wang, Y., J. Wang, G. Han, C. Du, Y. Sun, L. Du, M. An, G. Yin, Y. Gao and Y. Song, Superior catalytic performance and CO tolerance of Ru@Pt/C-TiO2 electrocatalyst toward methanol oxidation reaction. Applied Surface Science, 2019. **473**: p. 943-950.
58. Sun, Y., Y. Zhou, Y. Liu, Q. Wu, M. Zhu, H. Huang, Y. Liu, M. Shao and Z. Kang, A photoactive process cascaded electrocatalysis for enhanced methanol oxidation over Pt-MXene-TiO 2 composite. Nano Research, 2020: p. 1-8.
59. Zhang, X., J. Zhang, H. Cao and Y. Li, Preparation of Pt/(Ti3C2Tx) y-(MWCNTs) 1-y electrocatalysts via a facile and scalable solvothermal strategy for high-efficiency methanol oxidation. Applied Catalysis A: General, 2019. **585**: p. 117181.
60. Yang, C., Q. Jiang, H. Huang, H. He, L. Yang and W. Li, Polyelectrolyte-Induced Stereoassembly of Grain Boundary-Enriched Platinum Nanoworms on Ti3C2T x MXene Nanosheets for Efficient Methanol Oxidation. ACS Applied Materials Interfaces, 2020. **12**(21): p. 23822-23830.
61. Anantharaj, S. and S. Kundu, Do the evaluation parameters reflect intrinsic activity of electrocatalysts in electrochemical water splitting?. ACS Energy Letters, 2019. **4**(6): p. 1260-1264.

62. Lee, S.W., S. Chen, W. Sheng, N. Yabuuchi, Y. Kim, T. Mitani, E. Vescovo, and Y. Shao-Horn, Roles of surface steps on Pt nanoparticles in electro-oxidation of carbon monoxide and methanol. Journal of the American Chemical Society, 2009. **131**(43): p. 15669-15677.
63. Xu, J., Y. Liu, J. Li, I. Amorim, B. Zhang, D. Xiong, N. Zhang, S.M. Thalluri, J.P.S. Sousa, and L. Liu, Hollow cobalt phosphide octahedral pre-catalysts with exceptionally high intrinsic catalytic activity for electro-oxidation of water and methanol. Journal of Materials Chemistry A, 2018. **6**(42): p. 20646-20652.
64. Fang, Y.-H. and Z.-P. Liu, Tafel kinetics of electrocatalytic reactions: from experiment to first-principles. ACS Catalysis, 2014. **4**(12): p. 4364-4376.
65. Liu, M., L. Kong, X. Wang, J. He, and B. Xian-He, Engineering bimetal synergistic electrocatalysts based on metal–organic frameworks for efficient oxygen evolution. Small, 2019. **15**(45): p. 1903410.
66. Wang, L., G. Zhang, Y. Liu, W. Li, W. Lu and H. Huang, Facile synthesis of a mechanically robust and highly porous NiO film with excellent electrocatalytic activity towards methanol oxidation. Nanoscale, 2016. **8**(21): p. 11256-11263.
67. Abdullah, N., S. Kamarudin, and L. Shyuan, Novel anodic catalyst support for direct methanol fuel cell: characterizations and single-cell performances. Nanoscale research letters, 2018. **13**(1): p. 90.
68. Ramirez, A.M., B.R. Camacho, M.V. Aguilera, I.R.G. Esquivel and Ramírez-Minguela, Effect of different zeolite as Pt supports for methanol oxidation reaction. Applied Surface Science, 2018. **456**: p. 204-214.

69. Shahrokhian, S. and S. Rezaee, Vertically standing Cu2O nanosheets promoted flower-like PtPd nanostructures supported on reduced graphene oxide for methanol electro-oxidation. Electrochimica Acta, 2018. **259**: p. 36-47.
70. Sha, R. and S. Badhulika, Facile synthesis of three-dimensional platinum nanoflowers decorated reduced graphene oxide: An ultra-high performance electro-catalyst for direct methanol fuel cells. Materials Science Engineering: B, 2018. **231**: p. 115-120.
71. Wang, R., M. Lou, J. Zhang, Z. Sun, Z. Li and P. Wen, ZIF-8@ ZIF-67-derived co embedded into nitrogen-doped carbon nanotube hollow porous carbon supported pt as an efficient electrocatalyst for methanol oxidation. Nanomaterials, 2021. **11**(10): p. 2491.
72. Sreenivasa, K.G., R.N. Ramamanohar, B. Sravani, S.L. Subramanyam, R.T. Veera, V. Madhavi, and R.S. Adinarayana, Ultra-range bimetallic Pt–Pd nanospheres deposited on reduced graphene sheet as efficient electrocatalyst towards electrooxidation of methanol. Journal of Cluster Science, 2021. **32**(1): p. 27-36.
73. Wagner, N. and E. Gülzow, Change of electrochemical impedance spectra (EIS) with time during CO-poisoning of the Pt-anode in a membrane fuel cell. Journal of Power Sources, 2004. **127**(1-2): p. 341-347.
74. Yuan, X., J.C. Sun, H. Wang, and J. Zhang, AC impedance diagnosis of a 500 W PEM fuel cell stack: Part II: Individual cell impedance. Journal of Power Sources, 2006. **161**(2): p. 929-937.
75. Thoufeeq, S., P.K. Rastogi, N. Sreekanth, M.M.R.I. Anantharaman and T.N. Narayanan, Nickel-reduced graphene oxide composite foams for electrochemical oxidation processes: towards biomolecule sensing. MRS Communications, 2018. **8**(3): p. 695-702.

76. Yahya, N., S.K. Kamarudin, N.A. Karim, S. Basri and A.M. Zainoodin, Nanostructured Pd-based electrocatalyst and membrane electrode assembly behavior in a passive direct glycerol fuel cell. Nanoscale Research Letters, 2019. **14**(1): p. 52.
77. Sarwar, E., T. Noor, N. Iqbal, Y. Mehmood, S. Ahmed and R. Mehek, Effect of Co-Ni ratio in graphene based bimetallic electro-catalyst for methanol oxidation. Fuel Cells, 2018. **18**(2): p. 189-194.
78. Bruno, M.M., M.A. Petruccelli, F.A. Viva and H.R. Corti, Mesoporous carbon supported PtRu as anode catalyst for direct methanol fuel cell: Polarization measurements and electrochemical impedance analysis of mass transport. International Journal of Hydrogen Energy, 2013. **38**(10): p. 4116-4123.